

Towards a Non-Stationary Correlated Fading Process for Diffuse Scattering in Ray Tracing

Benjamin Rainer, David Löschenbrand, Stefan Zelenbaba, Markus Hofer, and Thomas Zemen

Digital Safety & Security
Austrian Institute of Technology GmbH
Vienna, Austria
first.lastname@ait.ac.at

Abstract—In this paper we introduce the AIT ray tracer (RT) that is able to accurately simulate propagation effects of wireless communication channels. It covers the classical propagation mechanisms such as specular reflections, transmission and edge-diffraction. The novelty of our RT is that it allows to obtain correlated diffuse scattering and, thus, provides a time-variant Doppler spectral density. This is achieved by introducing a lattice-based surface tiling, which does not alter the position of the scattering points during simulation but provides high resolution diffuse scattering. The selection of the basis vectors for the finite lattice ensures that each ray falls into a separate delay bin (at least for first-order scattering). We implement our RT using the NVIDIA OptiX ray tracing engine, this enables us to trace a vast amount of rays in a single pass. We compare our RT simulations to a measurement conducted in a non-stationary urban intersection scenario achieving a near perfect match in terms of second order statistics.

Index Terms—ray tracing, channel modeling, diffuse scattering

I. INTRODUCTION

During the last decade channel modeling techniques like the geometry-based stochastic model (GSCM) [1] and ray tracing [2], [3] have gained a lot of attention. GSCMs use simplified ray tracing methods (e.g. 2D ray tracing, 2.5D ray tracing) and model the non line-of-sight components, such as those caused by diffuse scattering, penetration/refraction, and diffraction at edges by stochastic scatterers. The statistics of the scatterers' distributions are obtained through measurements. Due to their low complexity and high accuracy in predicting the (time-variant) wireless communication channel, GSCMs can be evaluated in real-time also allowing the emulation of the wireless channel [4].

The caveat of GSCMs is that once parameterized for a scenario it is only conditionally applicable to other scenarios, if at all. In this case ray tracing can show its strengths. It relies on physical models which describe the electro-magnetic wireless propagation effects, i.e., specular reflection(s), penetration, diffuse scattering and edge-diffraction. It uses a three dimensional model of the scenario which describes not only the geometry of the scenario but also the existing materials and their properties (i.e., permittivity, permeability, roughness, correlation length) [5]. The applications of a calibrated and validated RTs are, but are not limited to e.g., fingerprinting

for localization purposes, simulation of antenna placement for coverage planning, channel estimation of complex and time-variant scenarios (e.g., street canyon) and as ground truth for creating GSCMs.

A recent survey of existing ray-tracing tools is given in [2] which provides a comprehensive overview of existing commercial, academic and publicly available electromagnetic ray-tracing tools. The only RT in this survey which uses GPU(s) [6] is the RT by Wireless InSite [7]. The other RTs listed rely on other techniques for speeding up computation such as distributed computing, dimension reduction, multi-threading and space partitioning. A RT based on ray launching which is also implemented using NVIDIA OptiX is presented in [8]. Here the GPU is only used to determine which rays do arrive at the reception sphere. A scene query tree is constructed which allows for eliminating duplicate paths and the *frame coherence* is exploited by using directions that lead to the receiver(s) for the next time step when tracing non-stationary scenarios. However, the RT in [8] does not include diffuse scattering or other mechanism besides geometric optics and the uniform theory of diffraction (UTD) [9]. A very recent publicly available open source RT called Opal [10] provides interfaces for OMNet++ [11] (a discrete event simulator for communication networks) and to Unity [12] (a 3D game engine). However, it does not support diffuse scattering nor diffraction at its current development stage [13].

Current RTs produce reasonable matches in the power delay profile (PDP) for short delays. However, most RTs are not able to produce a PDP that captures the delay spread when compared to measurements [14] for longer delays which are caused by multiple diffuse reflections, especially in ultra wide-band scenarios [15]. A good matching PDP ensures that link-level simulations based on these ray-tracing results see a realistic received signal strength and delay spread. However, in non-stationary scenarios the performance of a communication system is also fundamentally influenced by the Doppler spread [16]. We define diffuse components in the PDP and DSD as the results of reflections which are not covered by Snell's law. In order to accurately predict the Doppler and delay spread it is desirable that not only line-of-sight (LOS) and diffracted components are modeled correctly, but also diffuse

components influence the resulting Doppler spread and Delay spread considerably. In this paper we present a RT which is capable of producing correlated fading processes not only for LOS and diffracted components but also, and most importantly, for diffuse scattering. The scientific contributions of this paper are as follows:

- We present a position invariant surface tiling method, which leads to a rich and correlated Doppler process.
- The proposed RT is validated by comparing simulation results to a measurement conducted in a non-stationary urban intersection scenario by means of second order statistics.

II. SURFACE TILING FOR DIFFUSE SCATTERING

Our RT follows a hybrid approach, combining analytic ray tracing and ray launching. Therefore, we first, identify possible reflection, diffraction, and diffuse interaction points analytically on surfaces without rigorous validity checks. Second, we launch rays towards these points in space using the NVIDIA OptiX ray engine ensuring that only non-blocked rays do hit the corresponding receiver. We support and implement the following mechanisms for identifying reflections, diffraction, and diffuse scattering on surfaces:

- 1) Reflection(s): The n -th order specular reflections computed by the image method, cf. (1) and their electromagnetic field is evaluated according to the Fresnel equations [17].
- 2) Diffraction: The edge diffraction is calculated according to the UTD [9].
- 3) Diffuse scattering: The points on surfaces for diffuse tiling are chosen according to [18] (rectangular), [19] (circular) and our novel tiling method based on lattices which we present in this section including the Lambertian and directive scattering model.

We assume that a surface is a subset of a sub-vector space. Specifically, surfaces in our RT are spanned by vectors $\mathbf{u}, \mathbf{v} \in \mathbb{R}^3$ and we further use its normal given by $\mathbf{n} = \mathbf{u} \times \mathbf{v}$, where \times denotes the outer/cross product. For the image method we compute the k -th reflection point for a given permutation of surfaces by the sequence given in (1), where \mathbf{p}_k denotes the k -th image of the receiver and \mathbf{a}_k denotes the surface center and $\mathbf{u}_k, \mathbf{v}_k$ the spanning vectors of the k -th surface. We obtain the direction for the n -th order reflection by $(\mathbf{p}_n - \mathbf{p}_t) / \|\mathbf{p}_n - \mathbf{p}_t\|_2$, where $\mathbf{p}_t \in \mathbb{R}^3$ denotes the position of the transmitter.

The diffuse tiling presented in [18], [20] recursively divides each surface into rectangular tiles by starting at four tiles and for each of these four tiles a recursion step is done by dividing it further until the termination condition is fulfilled. The termination condition is the far field assumption and the tiling for a tile is stopped if for a tile center $\mathbf{t}_c \in \mathbb{R}^3$ it holds that

$$\|\mathbf{t}_c - \mathbf{p}_t\|_2 > \frac{2\|(dx, dy)\|_\infty^2}{\lambda},$$

where $dx, dy \in \mathbb{R}^+$ denote the extent of the tile, $\mathbf{p}_t \in \mathbb{R}^3$ denotes the transmitter position, for $v \in \mathbb{R}^n$ $\|v\|_\infty := \max_{1 \leq i \leq n} \{|v_i|\}$ and λ denotes the wavelength in meters. This condition ensures that we can find a point on the surface which is not covered by the near field. This tiling does not take the system bandwidth into account and may generate scattering points which could fall into the same delay bin with respect to first order scattering. Another issue arises when we consider non-stationary scenarios. Scattering points which are not covered at time instant t_1 may be covered by the near field at another time instant t_2 , leading to the fact that certain sub-tiles are being further divided at time instant t_2 resulting in other scattering points (no continuous change in delay).

A circular tiling algorithm for diffuse scattering which considers the system bandwidth and aims on ultra-wide bandwidth scenarios is discussed in [19]. It was initially designed for ultra-wide band scenarios and ensures that each single first order diffuse path falls into a separate delay bin. The radius of the circular tiles is chosen by

$$r := \frac{c}{2B},$$

where c is the speed of light (299792458 m/s in vacuum) and B denotes the system bandwidth. The starting point for tiling is chosen at random on each surface and each tile center adds a random phase (uniformly drawn from $[0, 2\pi[$) to the impinging wave/ray. Furthermore, the initial starting point for tiling is uniformly chosen on the surface. In the comparison between the tiling algorithm we will also show that it further under/overestimates the area of a given surface.

Both methods [18], [19] do suggest to add an uniformly distributed phase $\phi \sim U([0, 2\pi[$ to the electro-magnetic field of the ray impinging on a scattering interaction point by multiplying it with a realization of $Z = e^{i\phi}$. We notice that computing the Doppler spectral density from the time- and frequency varying channel obtained by the sum of complex exponentials (cf. (7)) leads to uncorrelated diffuse scattering over time. The reason is the summation for a single time instant m and frequency bin q . The $c_{m,k}$ include the uniformly drawn phase for paths subject to diffuse scattering. The fact that $E\{Z\} = 0$ and for $\phi_k \sim_{\text{i.i.d.}} U([0, 2\pi[$, $S_n = \sum_{k=1}^n e^{i\phi_k}$ we have $E\{S_n\} = 0$. We further notice that $\arg(S_n) = \text{atan2}(\text{Im}(S_n), \text{Re}(S_n))$ is again uniformly distributed on $[0, 2\pi[$ and that its expectation is undefined.

A. Position Invariant Lattice-based Tiling

Definition 2.1: A lattice Λ^n is a subgroup of \mathbb{R}^n given by $\Lambda^n(\mathbf{b}_1, \dots, \mathbf{b}_n) := \{\sum_{i=1}^n \alpha_i \mathbf{b}_i : \alpha_i \in \mathbb{Z}\}$, where $\{\mathbf{b}_1, \dots, \mathbf{b}_n\} \subset \mathbb{R}^n$ is a basis.

In contrast to the existing tiling methods, we propose to cover a surface with a finite lattice (cf. Def.2.1) where we assign to each lattice point an area with respect to its position and depending on the given system bandwidth. We use the spanning vectors \mathbf{u}_i , $1 \leq i \leq n$, (which are linearly independent) and compute

$$\mathbf{p}_k = -\mathbf{p}_{k-1} + 2 \left[\begin{pmatrix} \mathbf{u}_k^T & \mathbf{v}_k^T \end{pmatrix} (1 - \langle \mathbf{u}_k, \mathbf{v}_k \rangle)^{-1} \begin{pmatrix} 1 & -\langle \mathbf{u}_k, \mathbf{v}_k \rangle \\ -\langle \mathbf{v}_k, \mathbf{u}_k \rangle & 1 \end{pmatrix} \begin{pmatrix} \langle \mathbf{p}_{k-1} - \mathbf{a}_k, \mathbf{u}_k \rangle \\ \langle \mathbf{p}_{k-1} - \mathbf{a}_k, \mathbf{v}_k \rangle \end{pmatrix} + \mathbf{a}_k \right] \quad (1)$$

an orthogonal unit basis $\{\mathbf{o}_1, \dots, \mathbf{o}_n\}$ using the Gram-Schmidt process. The i -th basis vector of the lattice reads as

$$\mathbf{b}_i = \mathbf{o}_i \frac{c}{2B}.$$

An increase in the system bandwidth leads to an increase in the number of scattering points. The selection of the basis results in a minimum distance of $\frac{c}{2B}$ and a maximum distance of $\frac{c}{\sqrt{2}B}$ between neighboring lattice points, and thus causing no overlap in the delay for first order diffuse scattering of neighboring points. In order to preserve the area of the surface we start at the surface's center and distribute the remaining area of the surface to the lattice points near the edges. This allows to pre-compute the tiles prior to ray tracing and once for all surfaces in the scene. Therefore, the scattering points remain the same throughout simulation independent of the transmitter/receiver movement and position.

However, during ray tracing we have to remove those points which do not fulfill the far field assumption. Therefore, we have to identify whether the surface (partly) lies within the near field. This is done by determining the nearest point of surface s to the transmitter (cf. (2)).

$$\mathbf{p}_s = \arg \min_{\mathbf{p} \in s} \|\mathbf{p}_t - \mathbf{p}\|_2, \quad (2)$$

Interpreting and solving (2) in a geometrical sense, we end up with the following solution. We project \mathbf{p}_t orthogonally onto the plane spanned by \mathbf{u} and \mathbf{v} which results in $\mathbf{z} = \mathbf{u}x_1 + \mathbf{v}x_2 + \mathbf{a}$. If the projection lies on the bounding plane we have $2|x_1| \leq 1$ and $2|x_2| \leq 1$. Otherwise, we have the case $2|x_1| > 1$ and $2|x_2| > 1$ which leads to $(x_1 \ x_2) = (\text{sgn}(x_1) \ \text{sgn}(x_2))$ (the nearest point is a corner of the surface). If those cases are not fulfilled \mathbf{p}_s is on one of two edges/corners. Therefore, we project $(\mathbf{u}^T \ \mathbf{v}^T)\mathbf{x}^T + \mathbf{a}$ onto:

$$P_{\mathbf{x}}(\mathbf{y}) = \begin{cases} \begin{pmatrix} \mathbf{n}^T & \mathbf{v}^T \end{pmatrix} \begin{pmatrix} y_1 & y_2 \end{pmatrix}^T + \mathbf{a} + \text{sgn}(x_1)\mathbf{u} & 2|x_1| > 1, \\ \begin{pmatrix} \mathbf{u}^T & \mathbf{n}^T \end{pmatrix} \begin{pmatrix} y_1 & y_2 \end{pmatrix}^T + \mathbf{a} + \text{sgn}(x_2)\mathbf{v} & \text{otherwise} \end{cases}.$$

Finally, we compute

$$\mathbf{p} = \begin{cases} \mathbf{v} \text{sgn}(y_2) \min\{|y_2|, \|\mathbf{v}\|_2\} + \mathbf{n}y_1 + \mathbf{a} + \text{sgn}(x_1)\mathbf{u} & 2|x_1| > 1, \\ \mathbf{u} \text{sgn}(y_1) \min\{|y_1|, \|\mathbf{u}\|_2\} + \mathbf{n}y_2 + \mathbf{a} + \text{sgn}(x_2)\mathbf{v} & \text{otherwise} \end{cases}.$$

We consider all *lattice* points for diffuse scattering which are within the bounding plane if $\|\mathbf{p}_t - \mathbf{p}\|_2 > 2\lambda$ for antennas with an active part shorter than λ . For antennas with an

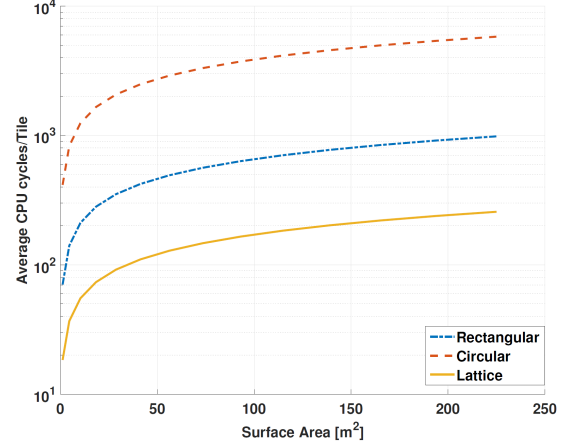


Fig. 1. Comparison of needed CPU cycles per tile as a function of the area.

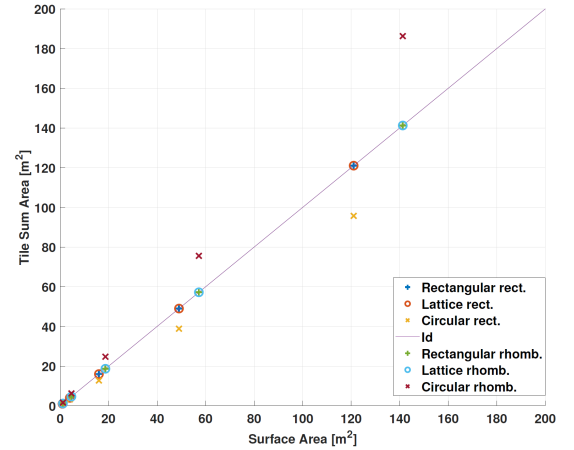


Fig. 2. Area covered by the tiling algorithms.

active part longer than λ we use $\|\mathbf{p}_t - \mathbf{p}\|_2 > \frac{2L^2}{\lambda}$, where L denotes the length of the antenna's active part. If the far field condition is not fulfilled, we exclude those lattice points from the valid scattering point set which lie within the near field. The projections can be pre-computed and are considerably faster than checking whether lattice points fall into the near field *sphere* (for a comparison on how fast the tiling is see Figure 1).

In order to model the electric field of diffuse reflections, we rely on the Lambertian and the directive diffuse scattering model [21]. Both models are evaluated according to a scattering coefficient $S_{\text{coeff}} \in [0, 1]$. The Lambertian model assumes that the radiation lobe of the scattered waves have their maximum in the direction orthogonal to the surface. The Lambertian scattering coefficient $L_{p,s}$ at point $\mathbf{p} \in \mathbb{R}^3$ and surface s is



Fig. 3. Crossing in Kaisermühlen 3D view (©Google).

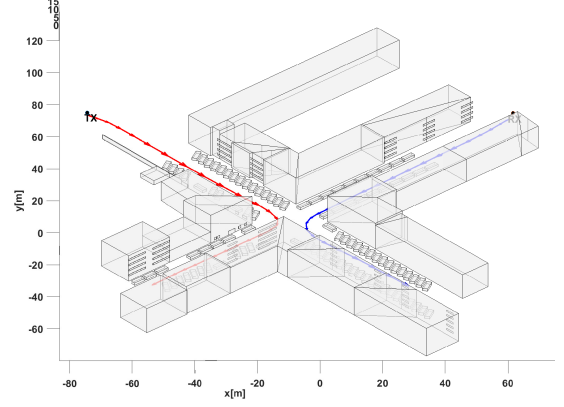


Fig. 4. Rebuilt scenario for RT of the crossing in Kaisermühlen. The red and blue trajectories denote the transmitter and receiver movement, respectively.

given as

$$L_{p,s} = \frac{S_{\text{coeff}} \cdot U}{d_{t,r}} \sqrt{\frac{dS \cos \theta_t \cos \theta_r}{\pi}}, \quad (3)$$

where $d_{t,r}$ is the total path length between receiver and transmitter (or between interaction points for higher diffuse scattering orders), dS denotes the area of the infinitesimal surface tile which corresponds to the point \mathbf{p} on surface s , θ_t denotes the angle between the surface normal, θ_r denotes the angle between the scattered and the reflected ray and $U = |\mathbf{E}_{\mathbf{p}}^{\text{ref}} / \mathbf{E}_{\mathbf{p}}^{\text{in}}|$ denotes the fraction of the incident ($\mathbf{E}_{\mathbf{p}}^{\text{in}}$) and reflected ($\mathbf{E}_{\mathbf{p}}^{\text{ref}}$) electric field. The directive model assumes that maximum energy is concentrated towards the specular reflection and thus its scattering attenuation coefficient $D_{p,s}$ is given as

$$D_{p,s} = \frac{S_{\text{coeff}} \cdot U}{d_{t,r}} \sqrt{\frac{dS \cos \theta_t}{F(\alpha_R)}} \left(\frac{1 + \cos \theta_r}{2} \right)^{\frac{\alpha_R}{2}}, \quad (4)$$

where $\alpha_R \in \mathbb{N}$ denotes the width of the scattering lobe and $F(\alpha_R)$ is defined as

$$F(\alpha_R) = \frac{1}{2^{\alpha_R}} \sum_{i=0}^{\alpha_R} \binom{\alpha_R}{i} I_i, \quad (5)$$

where I_i is defined as

$$I_i = \frac{2\pi}{i+1} \left(\cos \theta_t \sum_{k=0}^{i-1} \binom{2k}{k} \frac{\sin^{2k} \theta_t}{2^{2k}} \right)^{\frac{1-(-1)^i}{2}}. \quad (6)$$

Actually, the diffuse scattering coefficient is a function of $(dS, S_{\text{coeff}}, \theta_t, \theta_r, d_{t,r}, U)$, where U can also be obtained by the Fresnel equations. Since our diffuse tiling provides fixed tile sizes we precompute the scattering model before ray tracing obtaining a scattering coefficient that depends on $(\theta_t, \theta_r, d_{t,r}, U)$. We further attenuate $\mathbf{E}_{\mathbf{p}}^{\text{ref}}$ by

$$r_{\text{coeff}} = \sqrt{1 - S_{\text{coeff}}^2},$$

as given in [21]. This accounts for the proportion of the electric field that is scattered due to surface irregularities. The scattering coefficient S_{coeff} can also be derived from statistical parameters such as the correlation length (loosely formulated, the spatial frequency of the surface irregularities) and the roughness (the average height of surface irregularities) [22]. We select the phase for each scattering point uniformly in $[0, 2\pi[$ at the beginning of the simulation.

B. Tiling Performance

In order to show the benefit of our proposed tiling approach over the existing ones, we compare them with respect to CPU cycles per tile and surface area covered by the generated tiles. For comparison we use a rectangular and rhomboid surface varying its area. We conduct 1000 runs for each surface type, area and tiling algorithm using a system bandwidth of $B = 150$ MHz which determines the number of tiles/tile sizes for two of the investigated algorithms.

For the comparison we let all points fulfill the far field condition. Figure 1 depicts the average computational time in CPU cycles per tile as a function of the surface area. The circular tiling uses trigonometric functions for obtaining the centers of the tiles (rotation matrix) which has a significant impact on the performance, while the rectangular tiling performs better. The results show clearly that our lattice-based tiling outperforms the other two approaches.

Figure 2 depicts how much of the initial surface area is still covered by the generated tiles. We observe that for rectangular surfaces the circular tiling underestimates the area and for rhomboid surfaces we obtain an overestimation. The rectangular and lattice based tiling are able to cover the whole surface area but clearly differ in performance. The scattering coefficient which determines how much of the energy travels into the direction of the next scattering point or the receiver/transmitter is fundamentally determined by the size of the tile(s)/surface (cf. (3) and (4)). Thus, over- or underestimation may cause non realistic results in the PDP.

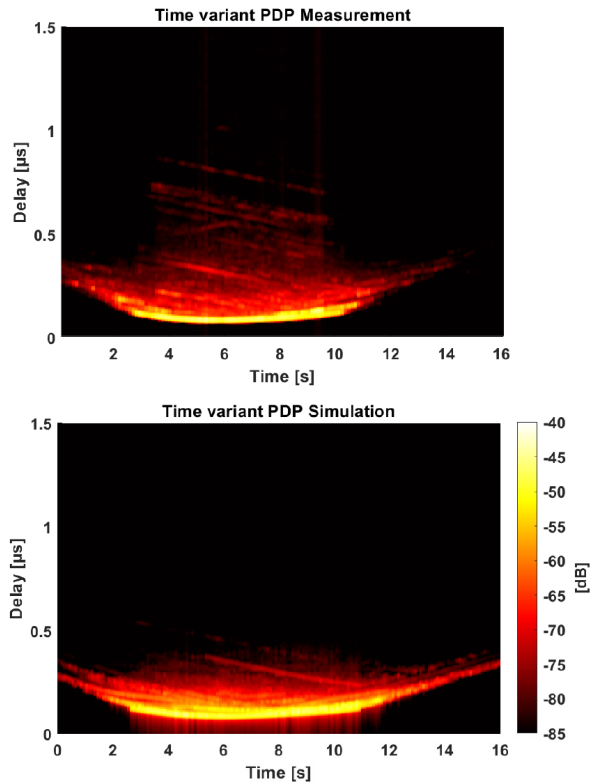


Fig. 5. PDP obtained by measurements and using our RT, respectively. For clarity of the presentation we omit the first ten seconds of the measurement and simulation.

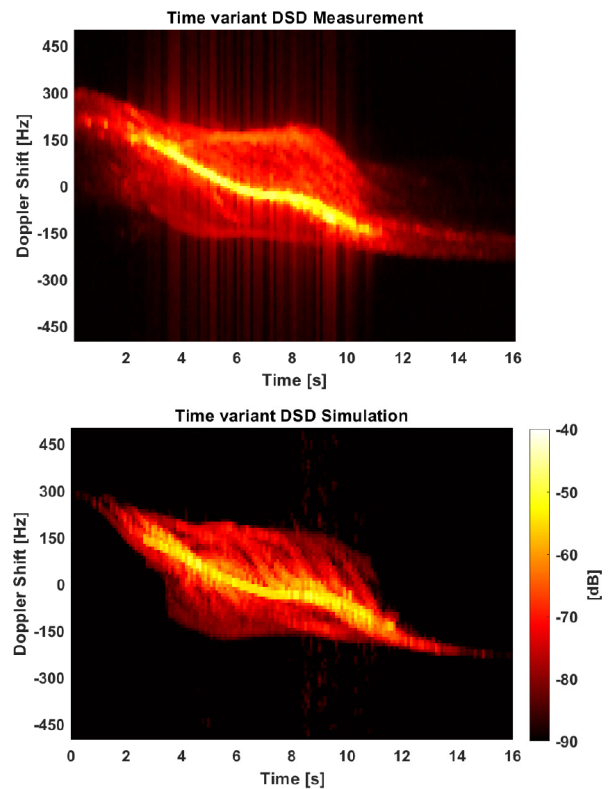


Fig. 6. DSD obtained by measurements and using our RT, respectively. For clarity of the presentation we omit the first ten seconds of the measurement and simulation.

C. Channel Model and Non-Stationarity

We model the time- and frequency variant channel transfer function with the sum of exponentials which reads as

$$h[m, q] = \sum_{k=1}^{N_m} c_{m,k} e^{-i2\pi\theta_{m,k}(f_c - \frac{B}{2} + q\Delta f)}, \quad (7)$$

where N_m is the number of paths received at time instant m , $q \in \{0, \dots, \lfloor \frac{B}{\Delta f} \rfloor\}$ with Δf being the subcarrier bandwidth, f_c the carrier frequency, $c_{m,k} \in \mathbb{C}$ the complex path gain at time m and the k -th path, $\theta_{m,k}$ the delay of the k -th path. For non-stationary scenarios we adopt the approach of assuming wide-sense stationary uncorrelated scattering for a short period of time t_s (stationary region) containing M samples such that $\|x_j(0) - x_j(M)\|_2 \leq \varepsilon_M \lambda \forall j \in G$ holds, where $j \in G$ is the j -th geometry object and G the set of objects in the scene, $x_j \in \mathbb{R}^3$ denotes the position of the j -th object, $\varepsilon_M \in \mathbb{N}$, λ the wavelength in meters [23]. Thus, during t_s we assume that the process is weak (wide-sense) stationary. The stationary duration then determines the Doppler shift resolution in Hz and is given by $\frac{1}{t_s}$. The one-sided maximum Doppler shift in Hz that can be captured by the simulation is then given by $\frac{M}{2t_s}$.

III. COMPARISON TO MEASUREMENTS

In order to validate the accuracy of our RT we use the data obtained by a measurement campaign conducted on a crossing in Kaisermühlen (Vienna, 48°13'40.7''N 16°25'22.7''E). The measurement has been conducted using the AIT multi-node channel sounder [24] with a bandwidth of $B = 150$ MHz at a center frequency of 5.9 GHz. The sub-carrier spacing is $\Delta f = 250$ kHz and the snapshot interval is 500 μ s. The scenario of the measurement campaign is provided in Figures 3 and 4. The traveled distance of transmitter and receiver is approximately 180m, respectively. The antennas are mounted on the transmitting node on a Toyota Prius at a height of approximately 1.4 m. For the receiving node we mount the antenna on a Volkswagen T5 at a height of 2 m. We use $\lambda/2$ dipole antennas for the measurement and the simulation.

We estimate the local scattering function (LSF) from the gathered discrete time- and frequency-varying channel transfer function (measurement and simulation) $h[m, q]$ according to [25] using a multi-taper estimate with I orthogonal time-domain and J orthogonal frequency-domain tapers. We collect S samples in time and $Q = 601$ samples in frequency per snapshot. The stationary region is indexed in time by $k_t \in \{1, \dots, \lfloor S/M \rfloor\}$ and in frequency by $k_f \in \{1, \dots, \lfloor Q/N \rfloor\}$ resulting in a region size of $M \times N$. For the measurement and

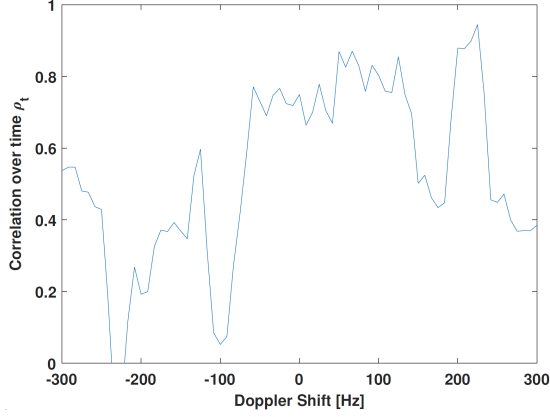


Fig. 7. Pearson correlation coefficient for each of the Doppler shift in [-300, 300] Hz over time.

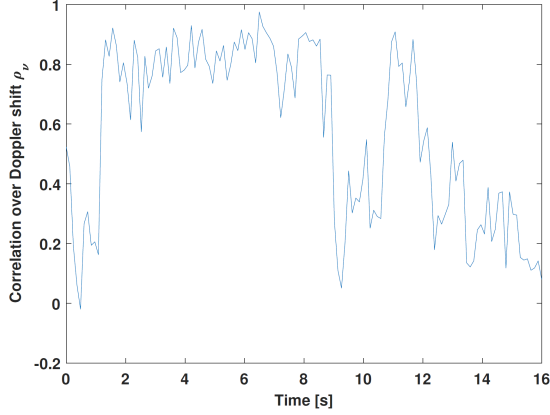


Fig. 8. Pearson correlation coefficient for each stationary region over the Doppler shift.

simulation we use a stationary time $t_s = 0.12$ s [26] and a stationary bandwidth of $f_{\text{stat}} = 150$ MHz. The time-varying PDP and DSD can be defined as the marginals of the LSF on the delay and Doppler axis, respectively, given as

$$P'_\tau[n; k_t, k_f] = \frac{1}{M} \sum_{p=0}^{M-1} C[n, p; k_t, k_f],$$

and, the DSD is

$$P'_\nu[p; k_t, k_f] = \frac{1}{N} \sum_{n=0}^{N-1} C[n, p; k_t, k_f].$$

We further investigate the delay spread and Doppler spread which read as

$$\sigma_\tau[k_t, k_f] = \sqrt{\frac{\sum_{n=0}^{N-1} (n\tau_s)^2 P'_\tau[n; k_t, k_f]}{\sum_{n=0}^{N-1} P'_\tau[n; k_t, k_f]} - \bar{\tau}[k_t, k_f]^2},$$

$$\bar{\tau}[k_t, k_f] = \frac{\sum_{n=0}^{N-1} (n\tau_s) P'_\tau[n; k_t, k_f]}{\sum_{n=0}^{N-1} P'_\tau[n; k_t, k_f]},$$

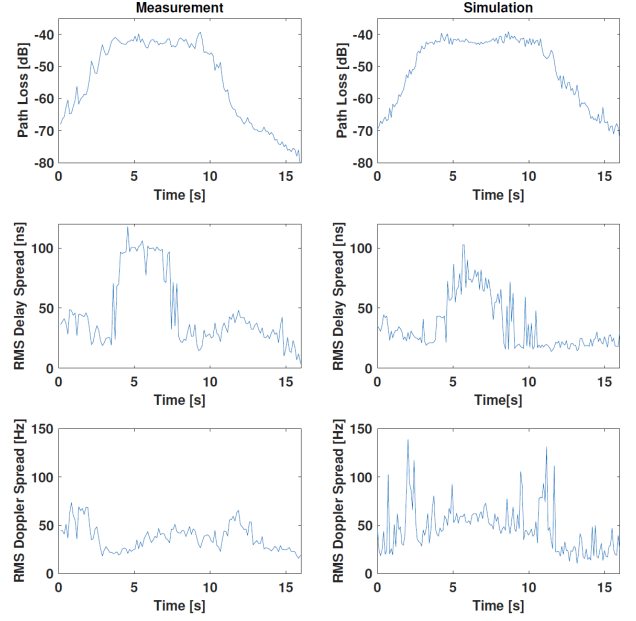


Fig. 9. Comparison of delay spread, Doppler spread and path loss over time between measurement and simulation.

and

$$\sigma_\nu[k_t, k_f] = \sqrt{\frac{\sum_{p=0}^{M-1} (p\nu_s)^2 P'_\nu[p; k_t, k_f]}{\sum_{p=0}^{M-1} P'_\nu[p; k_t, k_f]} - \bar{\nu}[k_t, k_f]^2},$$

$$\bar{\nu}[k_t, k_f] = \frac{\sum_{p=0}^{M-1} (p\nu_s) P'_\nu[p; k_t, k_f]}{\sum_{p=0}^{M-1} P'_\nu[p; k_t, k_f]},$$

where $\nu_s = 8.33$ Hz and $\tau_s = 6.67$ ns. In order to quantify how well the DSD of the simulation matches the measurement one, we rely on the Pearson correlation coefficient over time and frequency, which in its general form reads as

$$\rho(X, Y) = \frac{\sigma_{X,Y}}{\sigma_X \sigma_Y},$$

where X, Y are random variables, $\sigma_{X,Y} = \mathbb{E}\{(X - \mathbb{E}\{X\})(Y - \mathbb{E}\{Y\})\}$ is the covariance between X and Y , and σ_X denotes the standard deviation of X .

Figures 5 and 6 depict the PDP and DSD for the measurement and simulation, respectively. The trajectories for the transmitter and receiver have been collected during measurement, having a GPS sampling rate of 1 Hz. Thus, we assume a constant velocity between two sampling points. We interpolate the obtained GPS trajectories using splines, where we use the sampled GPS points as supporting points and interpolate points that are spaced according to the assumed stationary duration. Furthermore, there were objects, persons and moving cars which we do not model in the geometry. In addition to the PDP and DSD we investigate how well the obtained DSD by the simulation correlates with the one obtained by measurements (cf. Figures 7 and 8), a correlation coefficient > 0.6 denotes

a good correlation dependency. For the correlation over time we look at the Doppler frequencies [-300, 300] Hz. Figure 7 indicates that we achieve a good correlation with some lows for the Doppler frequencies lower than -100 Hz. This is caused by the missing diffuse components in the beginning and at the end. The root cause is the reduced complexity in geometry, missing moving objects and that we do not fade in/out diffuse scattering points. The same phenomena can be observed in Figure 8. In the beginning from 0 s until approx. 2 s, from approx. 9 s until 11 s, and starting from approx. 13 s until the end, the Pearson correlation coefficients experiences lows.

Figure 9 compares the delay spread, Doppler spread and path loss over time. In general, the simulation is able to capture the path loss very well. However, for the delay spread we see that our RT is able to reproduce the behavior but due to the trade-off in geometry we could not capture the delay spread to its full extent. For the Doppler spread we obtain a good match but the spikes in the beginning and in the end are due to edge diffractions which do not seem to be present in the measurement, mainly caused by cars modeled using cuboids.

IV. CONCLUSION

In this paper we propose a novel diffuse tiling for RT which is not only capable of reproducing PDPs with a good match but also provides a good matching Doppler and delay spread, correlated diffuse fading and a good matching Doppler spectral density. We validate the proposed RT by comparing simulations with measurements obtained in a non-stationary urban scenario. We showed quantitatively and qualitatively that the proposed tiling approach and the RT is able to accurately reproduce the measurements.

ACKNOWLEDGMENTS

This work is funded by the Austrian Research Promotion Agency (FFG) and the Austrian Ministry for Climate Protection, Energy, Transport, Innovation and Technology (BMK) within the project REALISM (864188) of the funding program transnational projects.

REFERENCES

- [1] J. Karedal, F. Tufvesson, N. Czink, A. Paier, C. Dumard, T. Zemen, C. F. Mecklenbrauker, and A. F. Molisch, "A geometry-based stochastic MIMO model for vehicle-to-vehicle communications," *IEEE Transactions on Wireless Communications*, vol. 8, no. 7, pp. 3646–3657, July 2009.
- [2] D. He, B. Ai, K. Guan, L. Wang, Z. Zhong, and T. Kürner, "The design and applications of high-performance ray-tracing simulation platform for 5G and beyond wireless communications: A tutorial," *IEEE Communications Surveys Tutorials*, vol. 21, no. 1, pp. 10–27, Firstquarter 2019.
- [3] M. Gan, G. Steinböck, Z. Xu, T. Pedersen, and T. Zemen, "A hybrid ray and graph model for simulating vehicle-to-vehicle channels in tunnels," *IEEE Transactions on Vehicular Technology*, vol. 67, no. 9, pp. 7955–7968, Sep. 2018.
- [4] M. Hofer, Z. Xu, D. Vlastaras, B. Schrenk, D. Loschenbrand, F. Tufvesson, and T. Zemen, "Real-time geometry-based wireless channel emulation," *IEEE Transactions on Vehicular Technology*, vol. PP, pp. 1–12, 2018.
- [5] T. Imai, "A survey of efficient ray-tracing techniques for mobile radio propagation analysis," *IEICE Transactions on Communications*, 2016.
- [6] Q. Huang, Z. Huang, P. Werstein, and M. Purvis, "GPU as a general purpose computing resource," in *2008 Ninth International Conference on Parallel and Distributed Computing, Applications and Technologies*, Dec 2008, pp. 151–158.
- [7] REMCOM, "Wireless InSite," accessed: 2019-04-15.
- [8] M. Schiller, A. Knoll, M. Mocker, and T. Eibert, "GPU accelerated ray launching for high-fidelity virtual test drives of vanet applications," in *2015 International Conference on High Performance Computing Simulation (HPCS)*, July 2015, pp. 262–268.
- [9] R. G. Kouyoumjian and P. H. Pathak, "A uniform geometrical theory of diffraction for an edge in a perfectly conducting surface," *Proceedings of the IEEE*, vol. 62, no. 11, pp. 1448–1461, Nov 1974.
- [10] E. Egea-Lopez, F. Losilla, J. Pascual-Garcia, and J. M. Molina-Garcia-Pardo, "Vehicular networks simulation with realistic physics," *IEEE Access*, vol. 7, pp. 44 021–44 036, 2019.
- [11] A. Varga and R. Hornig, "An overview of the OMNeT++ simulation environment," in *Proceedings of the 1st International Conference on Simulation Tools and Techniques for Communications, Networks and Systems & Workshops*, ser. Simutools '08, ICST, Brussels, Belgium, Belgium, 2008, pp. 60:1–60:10.
- [12] Unity Technologies, "Unity." [Online]. Available: unity.com
- [13] E. Egea-Lopez, "Opal," gitlab.com/esteban.egea/opal/tree/master, accessed: 2019-04-15.
- [14] T. Abbas, J. Nuckelt, T. Kürner, T. Zemen, C. F. Mecklenbräuker, and F. Tufvesson, "Simulation and measurement-based vehicle-to-vehicle channel characterization: Accuracy and constraint analysis," *IEEE Transactions on Antennas and Propagation*, vol. 63, no. 7, pp. 3208–3218, July 2015.
- [15] M. Gan, Z. Xu, M. Hofer, G. Steinböck, and T. Zemen, "A sub-band divided ray tracing algorithm using the DPS subspace in UWB Indoor Scenarios," in *2015 IEEE 81st Vehicular Technology Conference (VTC Spring)*, May 2015, pp. 1–5.
- [16] A. F. Molisch, *Wireless communications*. John Wiley & Sons, 2012.
- [17] R. Collin, *Foundations for Microwave Engineering*, ser. McGraw-Hill series in electrical engineering. McGraw-Hill, 1992.
- [18] F. Mani, F. Quitin, and C. Oestges, "Accuracy of depolarization and delay spread predictions using advanced ray-based modeling in indoor scenarios," *EURASIP Journal on Wireless Communications and Networking*, vol. 2011, no. 1, p. 11, Jun 2011.
- [19] M. Gan, X. Li, F. Tufvesson, and T. Zemen, "An effective subdivision algorithm for diffuse scattering of ray tracing," in *2014 URSI General Assembly and Scientific Symposium (URSI GASS)*, Aug 2014, pp. 1–4.
- [20] F. Mani, F. Quitin, and C. Oestges, "Directional spreads of dense multipath components in indoor environments: Experimental validation of a ray-tracing approach," *IEEE Transactions on Antennas and Propagation*, vol. 60, no. 7, pp. 3389–3396, July 2012.
- [21] V. Degli-Esposti, F. Fuschini, E. M. Vitucci, and G. Falciasecca, "Measurement and modelling of scattering from buildings," *IEEE Transactions on Antennas and Propagation*, vol. 55, no. 1, pp. 143–153, Jan 2007.
- [22] R. Piesiewicz, C. Jansen, D. Mittleman, T. Kleine-Ostmann, M. Koch, and T. Kurner, "Scattering analysis for the modeling of THz communication systems," *IEEE Transactions on Antennas and Propagation*, vol. 55, no. 11, pp. 3002–3009, Nov 2007.
- [23] G. Matz, "On non-WSSUS wireless fading channels," *IEEE Transactions on Wireless Communications*, vol. 4, no. 5, pp. 2465–2478, Sep. 2005.
- [24] S. Zelenbaba, D. Loeschenbrand, M. Hofer, A. Dakic, B. Rainer, G. Humer, and T. Zemen, "A scalable mobile multi-node channel sounder," *IEEE Wireless Communications and Networking Conference*, pp. 1–5, April 2020.
- [25] L. Bernadó, T. Zemen, A. Paier, J. Karedal, and B. H. Fleury, "Parametrization of the local scattering function estimator for vehicular-to-vehicular channels," in *2009 IEEE 70th Vehicular Technology Conference Fall*, Sep. 2009, pp. 1–5.
- [26] L. Bernadó, T. Zemen, F. Tufvesson, A. F. Molisch, and C. F. Mecklenbräuker, "The (in-) validity of the wssus assumption in vehicular radio channels," in *IEEE 23rd International Symposium on Personal, Indoor and Mobile Radio Communications - (PIMRC)*, Sep. 2012, pp. 1757–1762.